Title	Surface energy balance of snow cover in the Japanese Alps is similar to that in continental Alpine climates
Authors	Motoshi Nishimura, Akihiko Sasaki, Keisuke Suzuki
Citation	Environmental Research Communications, 3(5), 1-17, 2021
Issue Date	2021-5-10
Type	Journal Article
URL	https://doi.org/10.1088/2515-7620/abfcae
Right	
Textversion	publisher

ENVIRONMENTAL RESEARCH
COMMUNICATIONS

LETTER • OPEN ACCESS

Surface energy balance of snow cover in the Japanese Alps is similar to that in continental Alpine climates

Environmental Research Communications

LETTER

Surface energy balance of snow cover in the Japanese Alps is similar to that in continental Alpine climates

Motoshi Nishimura[1], **Akihiko Sasaki**[2] **and Keisuke Suzuki**[3]

[1] National Institute of Polar Research, Japan
[2] Department of Geography and Environmental Studies, Kokushikan University, Japan
[3] Faculty of Science, Shinshu University, Japan

E-mail: nishimura.motoshi@nipr.ac.jp

Keywords: surface energy balance, seasonal snow, snowmelt, alpine region

OPEN ACCESS

RECEIVED
1 February 2021

REVISED
27 April 2021

ACCEPTED FOR PUBLICATION
28 April 2021

PUBLISHED
10 May 2021

Abstract

The dynamics of a seasonal snow cover in the temperate cryosphere are critical for discussing climate change and understanding Earth systems. The most basic information is the previously unknown surface energy balance of snow and ice that can describe the snow dynamics in Japanese Alps. We show the surface energy balance properties of seasonal snow cover in the Northern Japanese Alps: one is the net radiation controlling the surface energy balance variation, and the negative latent heat flux (sublimation). We found that the surface energy balance property in this region is similar to that in the continental climate region due to the specific climate of Japan (winter monsoon) and topographic conditions (steep elevation gradient) of the Japanese Alps. This is a novel finding because Japanese seasonal snow cover is thought to accumulate and ablate under a maritime climate. It has been reported that the sensitivity of snow ablation to global warming depends on current atmospheric conditions. The results offer vital context for discussing environmental changes in the temperate cryosphere and environment of the Japanese Alpine region.

1. Introduction

Snow and ice cover on the Earth surface affect many other natural environment components. Because snow cover affects the energy and moisture exchanges between the atmosphere and the land surface (e.g. Cohen and Rind 1991), seasonal snow cover is a crucial factor in forming a local to global scale climate (Giorgi *et al* 1997, Mott *et al* 2015). Furthermore, a snow cover changes ground thermal regime due to the thermal insulation ability (Gądek and Leszkiewicz 2010), and conditions alpine vegetation phenology (Oguma *et al* 2019). The supply of snowmelt water causes fluctuations in river runoff (e.g. Suzuki 2017), and snowmelt induces natural disasters (e.g. Marks *et al* 1998). Therefore, to understand sub-systems in which the natural environment components interact with each other in a complex manner, it is necessary to clarify the accumulation-ablation process of snow cover.

Due to difficulties in obtaining *in situ* meteorological observations and integrating fragmented data, providing sufficient information for understanding the dynamics of the Japanese Alps and the advancement of environmental science are not adequate. Suzuki and Sasaki (2019) analysed long-term fluctuation of the meteorological condition and revealed that there is no significant trend of increasing air temperature in Japanese Alps. In addition, Kawase *et al* (2015), Suzuki (2017), and (Nishimura *et al* 2018, 2019) discussed an anticipated the snow or hydrological environment change in the Japanese Alps. Despite the existing research in this field, there is less knowledge based on detail *in situ* observation that in how climate condition the seasonal snow cover is accumulated and ablated in the Japanese Alps region.

Therefore, this study aims to understand the accumulation-ablation process of the seasonal snow cover in Japanese Alps and evaluate its impact on the scientific perspective. This study discussed the snow ablation process and control factors that impact the surface energy balance in the Northern Japanese Alps (Kamikochi, Norikura highland and Nishi-Hodaka). The snow surface energy balance is the most vital information in

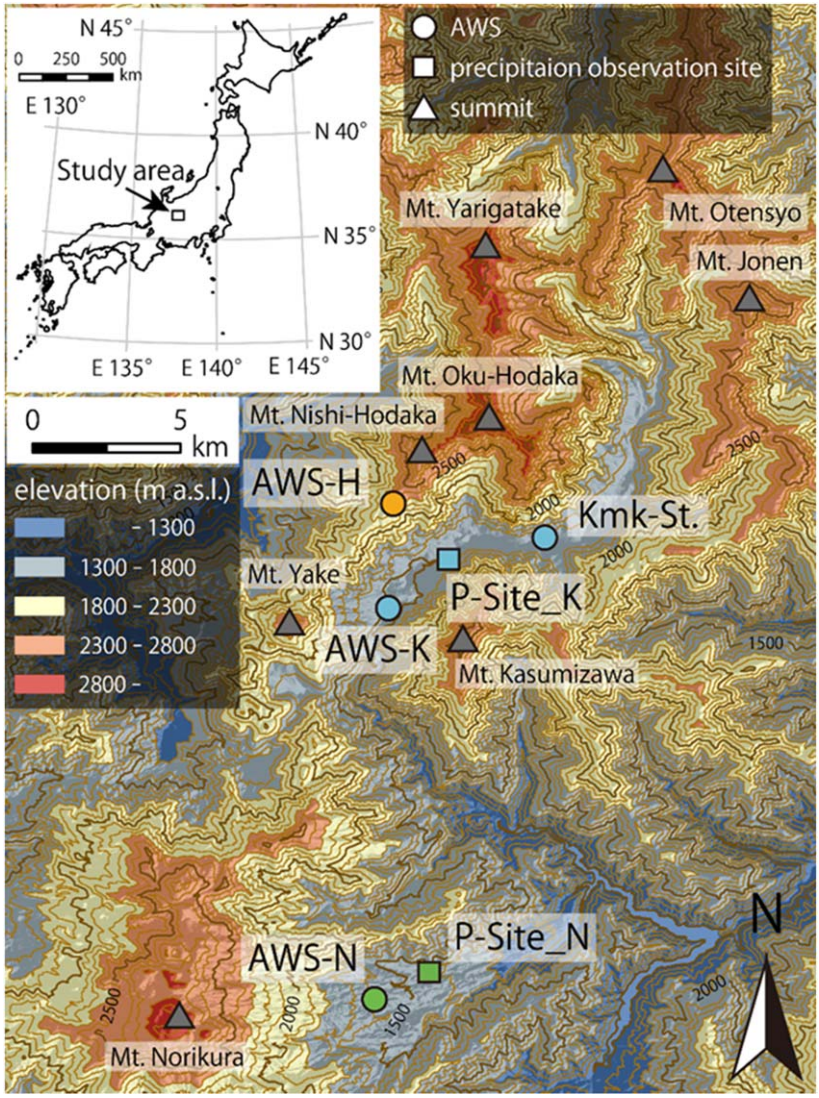

Figure 1. Map of meteorological observation sites: Kamikochi (AWS-K, blue symbols), Norikura highland (AWS-N, green symbols), and Nishi-Hodaka (AWS-H, orange symbol). Contour interval for thin lines is set as 100 m a.s.l., and that for thick lines is as 500 m a.s.l.

discussing snow accumulation-ablation processes. Through the analysis, we describe the mechanism of the mountain environmental system and the annual snow dynamics in the Japanese alpine region sat in the temperate cryosphere.

2. Method

2.1. Site description

The Japanese Alps are in central Japan (figure 1), and consist of several mountains with peaks of approximately 3000 m above sea level (a.s.l.) as part of the highest elevation range in Japan. There is a huge amount of snowfall in this region due to climatic and topographic factors. One is that, the Japanese Alps are part of the maritime climate because they are approximately 60 km from the coast of the Japan Sea, with a humid air mass quickly traveling to the mountains. Another is that the steep and high elevation terrain extends from the coast of the Japan Sea to the Japanese Alps. These characteristics make the Japanese Alps a unique landmass, as they feature glaciers and perennial snow patches despite lower elevation and in a more temperate climate than similar locations in the world that also have glaciers and snow patches (Fukui *et al* 2018, Arie *et al* 2019).

The mountainous members of the Northern Japanese Alps, Kamikochi, the Norikura highland, and Nishi-Hodaka were selected as study areas. Kamikochi is a generic term for the mountain area located in the southern part of the Northern Japanese Alps. Kamikochi is in the highland valley basin of the Azusagawa River at an elevation of 1500 m a.s.l. and is surrounded by approximately 3000 m a.s.l. high mountains in the Northern

Japan Alps. In the Kamkochi region, annual cumulative snowfall over 600 mm was often observed (Suzuki 2017) from 1981 to 2012 due to the strong winter monsoon, and seasonal snow cover formed every year. The Norikura highland is 10 km south of Kamikochi. Mt. Nishi-Hodaka-dake (2909 m a.s.l.) is one of the peaks of the Hodaka Mountain Range (including Mt. Kita-Hodaka-dake, Mt. Oku-Hodaka-dake and Mt. Mae-Hodaka-dake) extending from north to south. Nishi-Hodaka is approximately 3.8 km north of Kamikochi and tops the Kamikochi Valley ridge.

2.2. Meteorological observation

Shinshu University conducted meteorological observations at an automatic weather station (AWS) in Kamikochi (AWS-K; 1490 m a.s.l.), Norikura highland (AWS-N; 1590 m a.s.l.) and Nishi-Hodaka (AWS-H; 2355 m a.s.l.) (figure 1). All sites were in open locations. The AWS-K site was selected in the forest clearing location, and in AWS-H, there are fewer trees because AWS-H is located at an elevation of the tree line; therefore, the effect of weakening wind speed is minimal in those two sites. AWS-N is in open space, but there is forest surrounding (within 5–10 m away from) the site (Nishimura *et al* 2018, 2019).

The instrumental specifications of the AWSs are listed in table 1. Precipitation observations were not conducted in AWS-K and AWS-N; therefore, this study used the precipitation data from the nearest observation site (Kamikochi) of the Japan Meteorological Agency as AWS-K ('P-Site_K' in figure 1), and Nrk-St. that were operated by Shinshu University ('P-Site_N' in figure 1). The authors used the observed air temperature data of Kmk-St. that was also another AWS site operated by Shinshu University (figure 1) to calculate annual meteorological statistics. Only spring season precipitation data in AWS-H were used because no observations took place during winter in this location. Precipitation, whether rain or snow was classified using the threshold air temperature of 1.7 °C (Ogawa and Nogami 1994). Observed meteorological elements (see table 2) include air temperature (T_z) [°C], relative humidity (RH), wind speed (U) [m s^{-1}], wind direction (WD) [degree], atmospheric pressure (P) [hPa], incoming and reflected shortwave radiation (SW_{in} and SW_{ref}) [W m^{-2}], incoming and upward longwave radiation (LW_{in} and LW_{up}) [W m^{-2}], and snow depth (d) [m]. Every observation data was recorded in 10 min intervals. The snow depths in AWS-N and AWS-H were recorded every 60 min. The meteorological datasets were only analyzed for the snow-covered periods in 2016/17 winter, from 6 December 2016 to 4 May 2017 (AWS-K), from 24 November 2016 to 4 May 2017 (AWS-N), from 29 October 2016 to 2 July 2017 (AWS-H).

2.3. Surface energy balance model

The surface energy balance (SEB) [W m^{-2}] was determined using equation (1). The turbulent energy fluxes [W m^{-2}] were calculated using the bulk aerodynamic method from equations (4) and (5). The rainfall energy flux (Q_r) [W m^{-2}] was calculated using equation (6).

$$SEB = R_{net} + H + E + Q_r \tag{1}$$

$$R_{net} = SW_{in} - SW_{ref} + LW_{in} - LW_{up} \tag{2}$$

$$= SW_{in}(1 - \alpha) + \varepsilon LW_{in} - \sigma\varepsilon T_s{}^4 \tag{3}$$

$$H = \rho_a C_p C_H U(\theta_z - \theta_s) \tag{4}$$

$$E = \rho_a L_V C_E U(q_z - q_s) \tag{5}$$

$$Q_r = P_r \rho_w c_w (T_r - T_s) \tag{6}$$

where R_{net} is the net radiation, and H and E are the turbulent sensible and latent heat fluxes, respectively. R_{net} was calculated in equations (2) and (3), where SW_{in} is the incoming shortwave radiation, SW_{ref} is the reflected shortwave radiation, α is the surface albedo, LW_{in} is the incoming longwave radiation, LW_{up} ($=(1 - \varepsilon)\, LW_{in} + LW_{out}$) is the upward longwave radiation, LW_{out} is the outgoing longwave radiation from the snow surface, σ ($= 5.67 \times 10^{-8}$ [W m^{-2} K^{-4}]) is the Stefan-Boltzmann's constant, and ε ($= 0.98$) is the emissivity of the snow surface. In this study, surface temperature (T_s) [°C] was determined by outgoing longwave radiation using Stefan-Boltzmann's law. θ_z and θ_s is the potential temperature of the air and the snow surface, respectively. All energy fluxes toward the surface were defined as positive.

Turbulent energy fluxes were calculated using the bulk aerodynamic method (equations (4) and (5)). C_H and C_E are the bulk exchange coefficients for the sensible heat and latent heat fluxes, respectively, and ρ_a [kg m^{-3}] is the moist air density. C_p ($= 1.005$ [kJ K^{-1} kg^{-1}]) is the atmospheric specific heat at constant pressure, and L_V [J kg^{-1}] is the latent heat of evaporation or sublimation. When $T_s = 0$ °C, this study used Lv as the latent heat of evaporation ($Lv_{water} = 2505$ [kJ kg^{-1}]), and when $T_s < 0$ °C, this study used Lv as the latent heat of sublimation ($Lv_{ice} = 2838$ [kJ kg^{-1}]). q_z and q_s [g kg^{-1}] are the atmospheric and surface-specific humidity, respectively. The bulk coefficients (C_H and C_E) were calculated in a following procedure, considering the atmospheric stability by the Monin-Obukhov stability length (L).

Table 1. Meteorological observation instruments used in automated weather stations in AWS-K (Kamikochi), AWS-N (Norikura) and AWS-H (Nishi-Hodaka).

AWS-K				
	observation components	instrument		accuracy
air temperature and relative humidity	air temperature	Vaisala	WXT520	± 0.3 °C
	relative humidity			± 3% (0%–90%RH) ± 5% (90%–100%RH)
atmospheric pressure	atmospheric pressure	Vaisala	WXT520	± 0.5 hPa (0 °C–30 °C) ± 1 hPa (−52 °C–60 °C)
radiation	shortwave radiation longwave radiation	KIPP and ZONEN	CNR 4	± 5% (daily sum) ± 10% (daily sum)
snow depth	snow depth	North one	KADEC21-SNOW	± 1 cm
wind speed and wind direction	wind speed	YOUNG	Model 05103 Wind Monitor	± 0.3 m s^{-1}
AWS-N				
	observation components	instrument		accuracy
air temperature and relative humidity	air temperature	Delta OHM	HD9817T1R	± 0.2℃
	relative humidity			± 2% (10%–90%RH) ± 2.5% (in the remaining range)
atmospheric pressure	atmospheric pressure	Delta OHM	HD9408T	± 0.5 hPa (20 °C)
radiation	shortwave radiation longwave radiation	KIPP & ZONEN	CNR 4	± 5% (daily sum) ± 10% (daily sum)
snow depth	snow depth	North one	KADEC21-SNOW	± 1 cm
wind speed and wind direction	wind speed	YOUNG	Model 05103 Wind Monitor	± 0.3 m s^{-1}
precipitation (Nrk-St.)	precipitation	Ota Keiki Seisakusho	34-HP-P (Tipping Bucket Type)	± 0.5 mm (under 20 mm) ± 3% (over 20 mm)
AWS-H				
	observation components	instrument		accuracy
air temperature and relative humidity	air temperature	Delta OHM	HD9817T1R	± 0.2 °C
	relative humidity			± 2% (10%–90%RH) ± 2.5% (in the remaining range)
atmospheric pressure	atmospheric pressure	Delta OHM	HD9408T	± 0.5 hPa (20 °C)
radiation	shortwave radiation longwave radiation	KIPP & ZONEN	CNR 4	± 5% (daily sum) ± 10% (daily sum)
snow depth	snow depth	North one	KADEC21-SNOW	± 1 cm
wind speed and wind direction	wind speed	YOUNG	Model 05103 Wind Monitor	± 0.3 m s^{-1}
precipitation	precipitation	Ota Keiki Seisakusho	34-HP-P (Tipping Bucket Type)	± 0.5 mm (under 20 mm) ± 3% (over 20 mm)

Bulk coefficients for neutral atmospheric conditions (C_{HN} and C_{EN}) were calculated using equations (7) and (8).

$$C_{HN} = \frac{\kappa^2}{[\ln(z_v/z_{0v})\ln(z_t/z_{0t})]} \tag{7}$$

$$C_{EN} = \frac{\kappa^2}{[\ln(z_v/z_{0v})\ln(z_e/z_{0e})]} \tag{8}$$

where κ (=0.41) is the von Karman constant, and z_v, z_t, and z_e are the measurement height (corrected by the snow depth (d)) of wind speed, air temperature, and relative humidity ($z_t = z_e$; because of using the same sensor) at each AWS site, and z_{0v}, z_{0t} and z_{0e} are the roughness length for momentum, temperature, and moisture, respectively. This study was set $z_{0v} = 2.3 \times 10^{-4}$ [m] (Kondo and Yamazawa 1986) as a constant

Table 2. Constants and variables used in this study.

Constant			
Symbol	Term	Value	Dimension
$a_{,e}$, a_t	numeric constants		dimensionless
b_e, b_t	numeric constants		dimensionless
c_e, c_t	numeric constants		dimensionless
C_p	specific heat of air	1005	$J\,kg^{-1}\,K^{-1}$
c_w	specific heat of water	4.21	$kJ\,K^{-1}\,kg^{-1}$
Lv_{water}	latent heat of evaporation	2505	$kJ\,kg^{-1}$
Lv_{ice}	latent heat of sublimation	2838	$kJ\,kg^{-1}$
ε	emissivity of snow surface	0.98	dimensionless
σ	Stefan-Boltzmann constant	5.67×10^{-8}	$W\,m^{-2}\,K^{-4}$
κ	von Karman constant	0.41	dimensionless
ρ_w	water density	1000	$kg\,m^{-3}$
z_{0v}	roughness length for momentum	2.3×10^{-4}	m
Variable			
Symbol	Term		Dimension
C_E	bulk transfer coefficient of latent heat		dimensionless
C_{EN}	neutral bulk transfer coefficient of latent heat		dimensionless
C_H	bulk transfer coefficient of sensible heat		dimensionless
C_{HN}	neutral bulk transfer coefficient of sensible heat		dimensionless
d	snow depth		m
E	latent heat flux		$W\,m^{-2}$
H	sensible heat flux		$W\,m^{-2}$
L	Obukhov stability length		m
Lv	latent heat of water or ice		$J\,g^{-1}$
LW_{in}	incoming longwave radiation		$W\,m^{-2}$
LW_{net}	net longwave radiation		$W\,m^{-2}$
LW_{out}	outgoing longwave radiation		$W\,m^{-2}$
LW_{up}	upward longwave radiation		$W\,m^{-2}$
P	atmospheric pressure		Pa
P_r	rainfall intensity		$m\,s^{-1}$
Q_r	rainfall energy flux		$W\,m^{-2}$
q_z	atmospheric specific humidity		$g\,g^{-1}$
q_s	specific humidity of snow surface		$g\,g^{-1}$
q_*	turbulent moisture scale		$g\,g^{-1}$
R_{net}	net radiation		$W\,m^{-2}$
Re	roughness Reynolds number		dimensionless
RH	relative humidity		dimensionless
SEB	surface energy balance		$W\,m^{-2}$
SW_{in}	incoming shortwave radiation		$W\,m^{-2}$
SW_{net}	net shortwave radiation		$W\,m^{-2}$
SW_{ref}	reflected shortwave radiation		$W\,m^{-2}$
T_z	air temperature		K
T_r	temperature of rain drop		K
T_s	surface temperature		K
U	wind speed		$m\,s^{-1}$
u_*	air shear velocity		$m\,s^{-1}$
WD	wind direction		degree
z_v	height of observation for wind speed		m
z_t	height of observation for air temperature		m
z_e	height of observation for relative humidity		m
z_{0t}	roughness length for temperature		m
z_{0e}	roughness length for moisture		m
ρ_a	moist air density		$g\,m^{-3}$
α	surface albedo		dimensionless
ζ	stability parameter		dimensionless
θ_z	atmospheric potential temperature		K
θ_s	potential temperature of snow surface		K
θ_*	turbulent temperature scale		K
ν	kinematic viscosity		$m^2\,s^{-1}$
Ψ_M, Ψ_T, Ψ_E	stability function		dimensionless

value. z_{0t} and z_{0e} are calculated in equations (9) and (10), following Andreas (1987):

$$\ln\left(\frac{z_{0t}}{z_{0v}}\right) = a_t + b_t \ln Re + c_t(\ln Re)^2 \tag{9}$$

$$\ln\left(\frac{z_{0e}}{z_{0v}}\right) = a_e + b_e \ln Re + c_e(\ln Re)^2 \tag{10}$$

$$Re = \frac{u_* z_{0v}}{\nu} \tag{11}$$

$$u_* = \frac{\kappa\, U}{\ln(z_v/z_{0v})} \tag{12}$$

where Re is the roughness Reynolds number, a_t, b_t, c_t, a_e, b_e, and c_e are the numeric constants, u_* [m s^{-1}] is the air shear velocity, and ν [m^2 s^{-1}] is the kinematic viscosity of air. Those numeric constants are given by Re, and then, C_{HN} and C_{EN} were calculated.

This study adjusted the bulk coefficients for atmospheric stability using the Monin-Obukhov stability length, as L [m] (van den Broeke *et al* 2005) shown in equation (13):

$$L = \frac{{u_*}^2}{\kappa\frac{q_z}{\theta_z}(\theta_* + 0.62\theta_z q_*)} \tag{13}$$

$$\theta_* = \frac{\kappa(\theta_z - \theta_s)}{\ln(z_t/z_{0t})} \tag{14}$$

$$q_* = \frac{\kappa(q_z - q_s)}{\ln(z_e/z_{0e})} \tag{15}$$

where θ_* [K] and q_* [g kg^{-1}] are the turbulent scales of temperature and moisture, respectively. The relationships between the stability parameters ζ $(=z/L)$ were determined, and the atmospheric stability was calculated as shown in (i) and (ii) (Dyer 1974). In the case of (i) or (ii), calculations were conducted using equations (16)–(18), and then, the stability functions (Ψ_M, Ψ_T, and Ψ_E) were calculated using ζ the calculated values for each observation height (z_v, z_t, and z_e).

(i) $\zeta > 0$ (stable atmospheric condition)

$$\Psi_M = \Psi_T = \Psi_E = 1 + 5\,\zeta \tag{16}$$

(ii) $\zeta < 0$ (unstable atmospheric condition)

$$\Psi_M = (1 - 16\,\zeta)^{-\frac{1}{4}} \tag{17}$$

$$\Psi_T = \Psi_E = (1 - 16\,\zeta)^{-\frac{1}{2}} \tag{18}$$

This study defined that when ζ is positive, the boundary layer is stable, and when ζ is negative, the boundary layer is unstable, and the neutral condition is defined $\zeta < |0.01|$. In the case of $\zeta \to \infty$, which means $L \to 0$, this study assumed no turbulence occurred in each time step.

u_*, θ_*, and q_* considering atmospheric stability were recalculated using following equations (19)–(21).

$$u_* = \frac{\kappa\, U}{[\ln(z_v/z_{0v}) - \Psi_M]} \tag{19}$$

$$\theta_* = \frac{\kappa(\theta_z - \theta_s)}{[\ln(z_t/z_{0t}) - \Psi_T]} \tag{20}$$

$$q_* = \frac{\kappa(q_z - q_s)}{[\ln(z_e/z_{0e}) - \Psi_E]} \tag{21}$$

Because L is a function of u_*, θ_*, and q_*, this study conducted an iteration loop between equations (13) and (16)–(21) until L was converged to within 0.001% of the previous value of L. Using the converged L, calculations in equations (16)–(18) were conducted. The values of C_H, C_E, H, and E were calculated using equations (4), (5), (22), and (23).

$$C_H = \frac{\kappa^2}{\{[\ln(z_v/z_{0v}) - \Psi_M][\ln(z_t/z_{0t}) - \Psi_T]\}} \tag{22}$$

Table 3. Annual mean air temperature [°C], the annual range of air temperature [°C], and their standard deviation (SD) in Kamikochi, Norikura, and Nishi-Hodaka, and annual cumulative precipitation [mm] and its standard deviation in Kamikochi and Norikura.

	Air temperature [°C]				Precipitation [mm]		
region	Kamikochi	Norikura	Nishi-Hodaka		Kamikochi	Norikura	Nishi-Hodaka
period	2010–2018	2003–2018	2010–2018		2007–2018	2007–2018	
annual mean	5.8	5.5	1.3	Annual cumulative	2692	1946	no data
SD	0.7	0.5	0.6	SD	283	278	no data
annual range	25.2	24.7	25.8		—	—	—
SD	1.1	1.2	1.4		—	—	—

$$C_E = \frac{\kappa^2}{\{[\ln(z_v/z_{0v}) - \Psi_M][\ln(z_e/z_{0e}) - \Psi_E]\}} \tag{23}$$

Rainfall energy flux is the sensible heat supplied by raindrops. Q_r was calculated using equation (6). P_r [m s^{-1}] is the rainfall intensity, ρ_w (=1000 [kg m^{-3}]) is the density of the water, c_w (= 4.21 [kJ K^{-1} kg^{-1}]) is the specific heat capacity of the water, and T_r is the temperature of a rain drop, which is considered equal to T_z in this study. This study neglected the subsurface energy flux because its contribution to the surface energy balance is small (e.g. Andreassen *et al* 2008, Sicart *et al* 2008). In addition, this assumption is applied widely during the ablation period, because the entire snowpack is assumed to be 0 °C in that period. Therefore, this study discussed the results of surface energy balance analysis during the ablation period (in table 5 and figure 4).

3. Result

3.1. Meteorological observation data

The annual mean air temperature and the annual amount of precipitation in Kamikochi, Norikura, and Nishi-Hodaka are shown in table 3. However, annual precipitation was not calculated because all year precipitation observations in AWS-H were not conducted. The annual mean air temperatures in Kamikochi, Norikura, and Nishi-Hodaka were 5.8 °C, 5.5 °C, and 1.3 °C, respectively. The annual ranges of air temperature in Kamikochi, Norikura, and Nishi-Hodaka were 25.7 °C, 24.7 °C, and 26.0 °C, respectively. The annual cumulative precipitation in Kamikochi and Norikura were 2692 mm and 1946 mm, respectively.

Meteorological observation data during the snow-covered period of 2016/17 in AWS-K, AWS-N, and AWS-H are shown in figure 2. The air temperature difference between AWS-K and AWS-N was small, and a similar fluctuation of air temperature in AWS-K and AWS-N was observed. The air temperature in AWS-H was lower than that in the other two sites, reflecting a difference in the elevation of the AWS location. The positive air temperature was observed after early April in AWS-K and AWS-N, and after late April AWS-H. No noticeable differences in specific humidity were found. However, the specific humidity in the AWS-H was slightly higher than that in the other both sites. The fluctuation in specific humidity at all sites was similar. The wind speed at AWS-H was higher than that in the other two sites, and the wind speed in AWS-N was slightly lower than that in AWS-K. The mean wind speed during the snow-covered period in AWS-H was over 2.5 times higher than that in the other two sites. The snow depth in AWS-H was much larger than that in the other two sites. The maximum snow depths in 2016/17 in AWS-H, AWS-K, and AWS-N were 676 cm, 165 cm and 159 cm, respectively. Decreasing snow depth was observed in all sites after early April.

3.2. Surface energy balance analysis

All locations showed distinct surface energy balance properties, those were (1) net shortwave radiation controlled *SEB* variation and (2) an energy loss due to negative latent heat flux. The analysis of the surface energy balance during the ablation period is shown in table 4, and the energy flux in figure 3. The figures showing each energy balance component's contribution ratio in the text and table 4 were calculated by dividing an energy flux (e.g., net shortwave radiation, net longwave radiation) by the total energy flux (*SEB*). Net shortwave radiation is the most dominant energy source at all sites (over 100%), and the second major energy flux was the sensible heat flux. Net longwave radiation was the largest source of energy loss at all sites. Latent heat flux was the second source of energy loss at AWS-K and AWS-N, but it was the third largest source of positive energy flux at AWS-H. Rainfall energy flux hardly contributed to the snow ablation at all sites. This resulted in a radiation component that controlled the surface energy balance variation and snow ablation process.

The trends observed at each site can be summarized as follows: The surface energy balance was controlled by net shortwave radiation in AWS-K, which is 155.3% against *SEB*. The other significant energy flux was the sensible heat flux (30.8%). The net longwave radiation and latent heat flux were the energy sink and cooled the

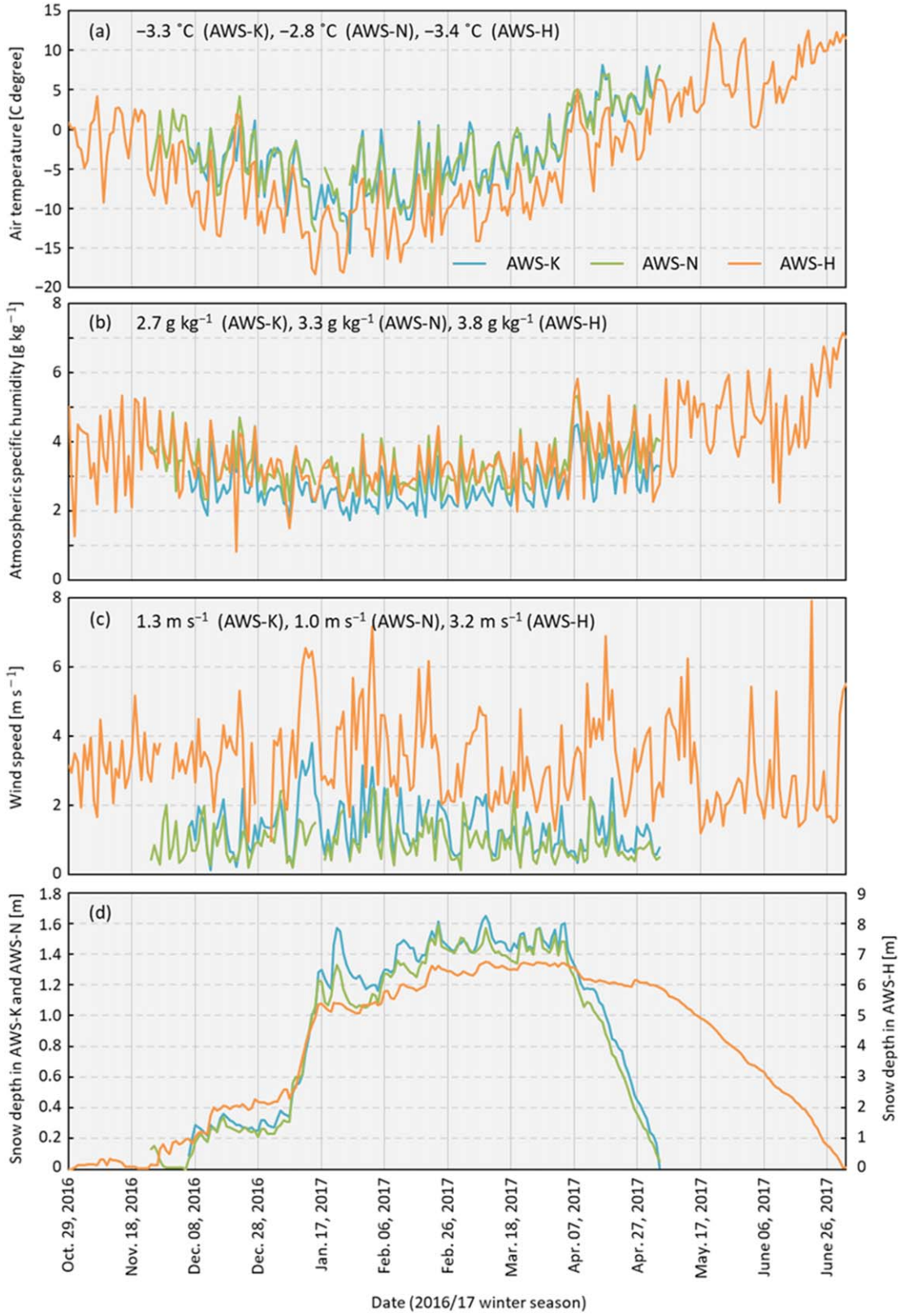

Figure 2. Result of meteorological observation in AWS-K (Kamikochi), AWS-N (Norikura), and AWS-H (Nishi-Hodaka); daily mean (a) air temperature [°C], (b) atmospheric specific humidity [g kg^{-1}], (c) wind speed [m s^{-1}] and (d) snow depth [cm] in snow-covered period. Figures in each graph are averaged values for the snow-covered period.

snow surface at −70.6% and −19.9%, respectively. The energy loss due to longwave radiation emission and latent heat flux in AWS-K was more extensive than that of the other two sites. The rainfall energy flux was a small source of energy (1.9%).

Table 4. Result of energy balance analysis for the ablation period in AWS-K (Kamikochi), AWS-N (Norikura), and AWS-H (Nishi-Hodaka). Respective energy flux for monthly mean and average of snow-covered periods are shown on the left. The values in parentheses show the proportion of *SEB* (Q_M). Figures in the month with '*' showing those figures do not meet statistical significance due to a data shortage.

			SEB		Net shortwave radiation		Net longwave radiation		Sensible heat flux		Latent heat flux		Rainfall energy flux	
			W m^{-2}	(%)	W m^{-2}	(%)	W m^{-2}	(%)	W m^{-2}	(%)	W m^{-2}	(%)	W m^{-2}	(%)
AWS-K	Feb.		8.5	(100.0)	28.3	(331.2)	−20.3	(−237.4)	7.7	(89.9)	−6.4	(−75.2)	0.2	(2.3)
	Mar.		16.0	(100.0)	43.0	(268.6)	−26.1	(−163.1)	6.0	(37.5)	−8.1	(−50.4)	0.0	(0.0)
	Apr.		76.8	(100.0)	85.1	(110.8)	−19.9	(−25.9)	13.6	(17.7)	−4.7	(−6.1)	2.2	(2.9)
	May	*	175.9	(100.0)	170.8	(97.1)	−12.1	(−6.9)	17.3	(9.9)	−0.3	(−0.2)	0.1	(0.1)
	June		—	—	—	—	—	—	—	—	—	—	—	—
	July		—	—	—	—	—	—	—	—	—	—	—	—
	ALL		28.0	(100.0)	43.4	(155.3)	−19.7	(−70.6)	8.6	(30.8)	−5.6	(−19.9)	0.5	(1.9)
AWS-N	Feb.		17.6	(100.0)	28.7	(162.8)	−15.3	(−86.9)	5.4	(30.9)	−1.3	(−7.6)	0.0	(0.0)
	Mar.		37.7	(100.0)	58.9	(156.2)	−24.1	(−63.8)	4.8	(12.7)	−3.8	(−9.9)	0.0	(0.0)
	Apr.		95.7	(100.0)	100.5	(104.9)	−14.5	(−15.1)	8.3	(8.6)	0.0	(0.0)	0.9	(0.9)
	May	*	147.7	(100.0)	147.4	(99.9)	−13.4	(−9.1)	10.8	(7.3)	2.2	(1.5)	0.6	(0.4)
	June		—	—	—	—	—	—	—	—	—	—	—	—
	July		—	—	—	—	—	—	—	—	—	—	—	—
	ALL		36.9	(100.0)	48.4	(131.3)	−17.2	(−46.6)	5.9	(15.9)	−1.2	(−3.3)	0.2	(0.6)
AWS-H	Feb.		19.4	(100.0)	42.5	(218.7)	−25.3	(−130.0)	1.2	(6.2)	0.1	(0.4)	No Data	No Data
	Mar.		26.7	(100.0)	43.3	(162.0)	−19.2	(−71.7)	1.9	(7.1)	−0.9	(−3.4)	No Data	No Data
	Apr.		72.4	(100.0)	96.2	(132.8)	−30.1	(−41.6)	6.1	(8.5)	−2.2	(−3.1)	1.0	(1.3)
	May		192.4	(100.0)	177.7	(92.3)	−11.5	(−6.0)	19.7	(10.2)	5.8	(3.0)	0.8	(0.4)
	June		225.5	(100.0)	181.7	(80.6)	−1.5	(−0.6)	25.1	(11.1)	18.4	(8.2)	1.7	(0.8)
	July	*	311.8	(100.0)	23.0	(7.4)	65.2	(20.9)	77.1	(24.7)	98.3	(31.5)	48.1	(15.4)
	ALL		80.8	(100.0)	87.7	(108.6)	−18.4	(−22.8)	8.0	(9.9)	2.2	(2.7)	0.8	(1.0)

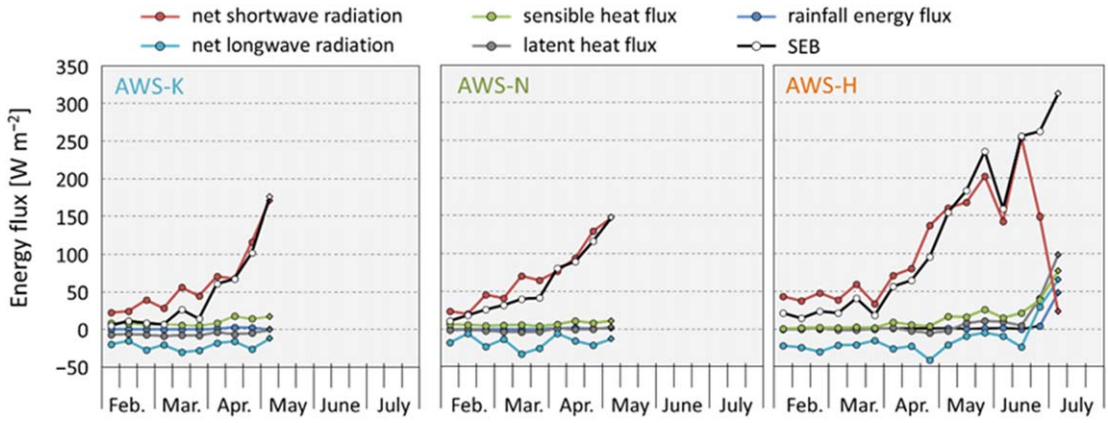

Figure 3. Result of energy balance analysis in AWS-K (Kamikochi), AWS-N (Norikura), and AWS-H (Nishi-Hodaka). A month is divided into three parts, which are the first ten days of the month (1st to 10th), followed by the next ten days (11th to 20th), and finally the remainder of the month (21st to the end of the month), and variation of each energy component shown. Data plot symbol represented by a diamond does not meet statistical significance due to a data shortage.

The surface energy balance property in AWS-N was similar to that in AWS-K. The largest energy source was net shortwave radiation (131.3%), and the second was a sensible heat flux (15.9%). In contrast, the greatest energy sink was net longwave radiation (−46.6%), followed by the latent heat flux (−3.3%). The rainfall energy flux was also a small positive energy source (0.6%).

The surface energy balance property at AWS-H was also similar to those in AWS-K and AWS-N. However, the amount of net shortwave radiation (108.6%) and the sensible heat flux (9.9%) were larger than those of AWS-K and AWS-N. Latent heat flux was negative in March and April (slightly positive in February), and then it turned to positive between May and July.

4. Discussion

4.1. Surface energy balance in Northern Japanese Alps region

We evaluated the surface energy balance properties for the Northern Japanese Alps: (1) net radiation that controlled the surface energy balance variation, and (2) negative latent heat flux (sublimation) in the mid-winter season. Net radiation contributed significantly (over 80%) to snow ablation in the Northern Japanese Alps, due to high net shortwave radiation (over 100%). The ablation-dominating shortwave radiation (e.g. Greuell and Smeets 2001) has been reported on by many previous studies. Therefore, a special snow ablation mechanism could not be recognized in the Northern Japanese Alps.

The surface energy balance properties of (1) and (2) described above were similar to continental climate regions (Willis *et al* 2002), suggesting that the snow cover was ablates in relatively dry atmospheric conditions during the winter season. Shortwave radiation increases due to less cloud formation (Abermann *et al* 2019) and energy sink in sublimation from snowpack when it is dry (Sicart *et al* 2005). The Japanese climate is considered maritime; therefore, there are reports on surface energy balance analyses for maritime climates (e.g. Matsumoto *et al* 2010). However, the surface energy balance property in continental climate region noted in Sicart *et al* (2005) was also confirmed in this study region in the mid-winter season.

This study reviewed previous reports and classified the surface energy balance according to continental or maritime climate (partly referring to Willis *et al* (2002) and Giesen *et al* (2008)). The results of the review are shown in table 5 and figure 4. The surface energy balance analysis data of this study listed in table 5 are only for the ablation period. Radiation elements are generally dominant (e.g. Sicart *et al* 2005) in continental climate region, and turbulent energy flux, in contrast, dominates the surface energy balance (e.g. Gillett and Cullen 2011). Data in this study listed in table 5 are similar to the surface energy balance property one expects of a continental climate region. Accumulated and ablated snow cover in relatively dry atmospheric, continental climate, conditions in this study are a new description, because the Japanese seasonal snow cover accumulation and ablation was generally thought to be governed by the maritime climate.

The high humidity air mass is advected to Japan caused by the East Asian monsoon, and steep elevation gradients in the region from the coast of the Sea of Japan to the Japanese Alps formed the dry atmospheric conditions (see figure 5). A warm and humid air mass from the Eurasian continent is supplied to the coastal area of the Sea of Japan (Magono *et al* 1966) due to three factors:

Table 5. Data used from the previous study in figure 4: study location, latitude, altitude, climate classification, observation period, and the surface energy balance.

Location					Observation Period						Surface Energy Flux (%)			References
Site	Country	Latitude	Altitude (m)	Climate							R_{net}	H	E	
Kamikochi	Japan	36° N	1490		Apr.	2017	—	May	2017		85	16	−4	this study
Norikura	Japan	36° N	1590		Feb.	2017	—	May	2017		92	10	−3	this study
Nishi-Hodaka	Japan	36° N	2355		Mar.	2017	—	Jul.	2017		83	11	5	this study
Peyto Glacier, Alberta	Canada	51° N	2500	Continental	Jun.	1988	—	Jul.	1988		51	42	7	Munro (1990)
Peyto Glacier, Alberta	Canada	51° N	2300	Continental	Jun.	1988	—	Jul.	1988		65	34	1	Munro (1990)
Peyto Glacier, Alberta	Canada	51° N	2510	Continental	Jul.	1970					44	48	8	Föhn (1973)
Hintereisferner	Austria	46° N	2500	Continental	Jul.	1986					91	10	−2	van de Wal *et al* (1992)
Hintereisferner	Austria	46° N	2630	Continental	Jul.	1989					93	20	−13	van de Wal *et al* (1992)
Niwot Ridge, CO	USA	40° N	3517	Continental	Apr.	1994	—	Jun.	1994		75	56	−31	Cline (1997)
Valee Blanche	France	45° N	3550	Continental	Jul.	1968					99	24	−23	De la Casiniere (1974)
St Sorline Glacier	France		2712	Continental	Aug.		—	Sep.	1969	and 1970	61	46	−1	Martin (1975)
Storglaciären	Sweden	68° N	1370	Maritime	Jul.	1994	—	Aug.	1994		66	30	5	Hock and Holmgren (1996)
Qamanârssûp sermia	Greenland	64° N	790	Maritime	Jun.	1980	—	Aug.	1986		67	38	−5	Braithwaite and Olesen (1990)
Ecology Glacier, King George Island	Antarctica	62° S	100	Maritime	Dec.	1990	—	Jan.	1991		64	29	7	Bintanja (1995)
Worthington Glacier, AK	USA	61° N		Maritime	Jul.	1967	—	Aug.	1967		51	29	21	Streten and Wendler (1968)
Worthington Glacier	Alaska	61° N	820	Maritime	Jul.	1967	—	Aug.	1967		51	29	20	Streten and Wendler (1968)
Qamanârssûp sermia	Greenland	61° N	880	Maritime	Jun.	1979	—	Aug.	1983		70	28	2	Braithwaite and Olesen (1990)
Lemon Creek Glacier	Alaska	58° N	1200	Maritime	Aug.	1968	—	Aug.	1968		48	43	9	Wendler and Streten (1969)
Kryoto Glacier	Russia	55° N	810	Maritime	Aug.	2000	—	Sep.	2000		33	44	23	Konya *et al* (2004)
Hodges Glacier	South Georgia	54° S	375	Maritime	Nov.	1973	—	Apr.	1974		55	48	−3	Hogg *et al* (1982)
Glacier Lengua	Chile	53° S	450	Maritime	Feb.	2000	—	Apr.	2000		35	54	7	Schneider *et al* (2007)
Tyndall Glacier	Chile	51° S	700	Maritime	Dec.	1993					51	42	7	Takeuchi *et al* (1995a, 1995b)
Moreno Glacier	Chile	50° S	330	Maritime	Nov.	1993					54	49	−4	Takeuchi *et al* (1995a, 1995b)
Ampere Glacier	Kerguelen Island	49° S		Maritime	Jan.	1972	—	Mar.	1972		58	25	16	Poggi (1977)
Soler Glacier	Chile	46° S	378	Maritime	Nov.	1985					57	43	−1	Fukami and Naruse (1987)
Brewster Glacier	New Zealand	44° S	1770	Maritime	Dec.	2007	—	Mar.	2008		52	25	20	Gillett and Cullen (2011)
Brewster Glacier	New Zealand	44° S	1760	Maritime	Oct.	2010	—	Sep.	2012		64	23	11	Cullen and Conway (2015)
Brewster Glacier	New Zealand	44° S	1760	Maritime	Oct.	2010	—	Sep.	2012		37	53	3	Conway and Cullen (2016)
Franz Josef Glacier	New Zealand	43° S		Maritime	Feb.	1990					21	55	25	Ishikawa *et al* (1992)
Mount Cook National Park	New Zealand	43° S		Maritime	Oct.	1995	—	Nov.	1995		63	27	4	Neale and Fitzharris (1997)
Temple Basin	New Zealand	42° S	1450	Maritime	Oct.	1982	—	Nov.	1982		16	57	25	Moore and Owens (1984)
Niigata	Japan	37° N	360	Maritime	Dec.	2007	—	Apr.	2008		80	16	3	Matsumoto *et al* (2010)
Blue Glacier, WA	USA			Maritime	Jul.	1958	—	Aug.	1958		69	25	6	La Chapelle (1959)

Table 5. (Continued.)

Location					Observation Period						Surface Energy Flux (%)			References
Site	Country	Latitude	Altitude (m)	Climate							R_{net}	H	E	
Location					Observation Period						Surface Energy Flux (%)			Reference
Site	Country	Latitude	Altitude (m)	Climate							R_{net}	H	E	
Berkner Island	Antarctica	79° S	886	Others	Feb.	1995	—	Dec.	1997	−91	108	−17		Reijmer *et al* (1999)
McCall Glacier	Alaska	69° N	1715	Others	Jun.	2004	—	Aug.	2004	74	25	5		Klok *et al* (2005)
Storglaciären	Sweden	67° N	1370	Others	Jul.	2000	—	Sep.	2000	55	32	13		Sicart *et al* (2008)
Vestari Hagafellsjökull	Iceland	64° N	500	Others	Jun.	2001	—	Aug.	2007	63	27	10		Matthews *et al* (2015)
Vestari Hagafellsjökull	Iceland	64° N	1100	Others	Jun.	2001	—	Aug.	2009	74	20	6		Matthews *et al* (2015)
West Gulkana Glacier	Alaska	63° N	1520	Others	Jun.	1986	—	Jul.	1986	57	35	8		Brazel *et al* (1992)
Storbreen	Norway	62° N	1600	Others	Jul.	1955	—	Sep.	1955	56	31	13		Liestøl (1967)
Storbreen	Norway	62° N	1570	Others	Sep.	2001	—	Sep.	2006	76	17	8		Giesen *et al* (2009)
Nordbogletscher	Greenland	61° N	880	Others	Jun.	1979	—	Aug.	1983	71	29	2		Braithwaite and Olesen (1990)
Omnsbreen	Norway	60° N	1540	Others	Jun.	1968	—	Sep.	1969	52	32	15		Messel (1971)
Midtdalsbreen	Norway	60° N	1450	Others	Oct.	2000	—	Sep.	2006	67	24	10		Giesen *et al* (2008)
Midtdalsbreen	Norway	60° N	1450	Others	Sep.	2001	—	Sep.	2006	66	25	11		Giesen *et al* (2009)
Pasterze	Austria	47° N	2205	Others	Jun.	1994	—	Aug.	1994	77	20	4		Greuell and Smeets (2001)
Pasterze	Austria	47° N	2310	Others	Jun.	1994	—	Aug.	1994	73	22	5		Greuell and Smeets (2001)
Pasterze	Austria	47° N	2420	Others	Jun.	1994	—	Aug.	1994	72	24	4		Greuell and Smeets (2001)
Pasterze	Austria	47° N	2945	Others	Jun.	1994	—	Aug.	1994	77	19	4		Greuell and Smeets (2001)
Pasterze	Austria	47° N	3225	Others	Jun.	1994	—	Aug.	1994	79	20	1		Greuell and Smeets (2001)
St Sorlin	France	45° N	2760	Others	Jul.	2006	—	Aug.	2006	84	22	−5		Sicart *et al* (2008)
Indian Himalaya	India	32° N	3050	Others	Jan.	2005	—	Apr.	2005	98	3	−1		Datt *et al* (2008)
Zongo Glacier	Bolivia	16° S	5050	Others	Nov.	1999	—	Dec.	1999	103	24	−27		Sicart *et al* (2008)

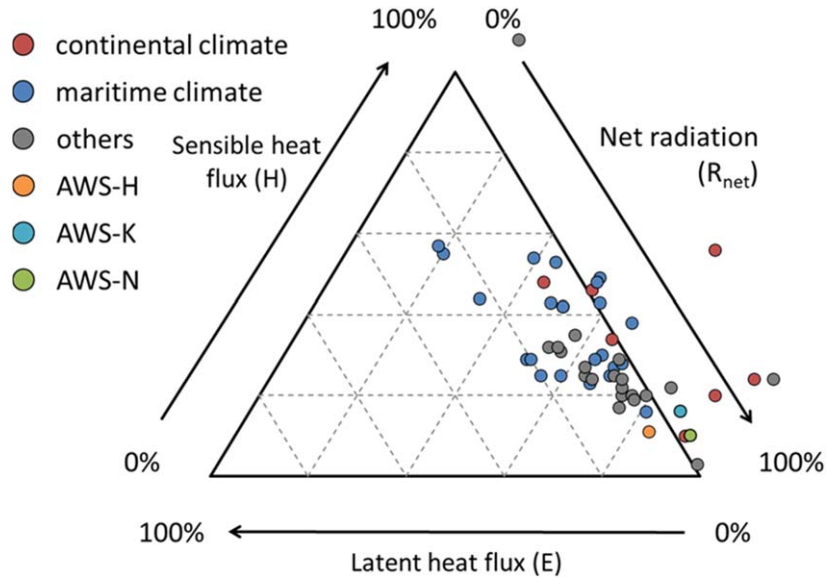

Figure 4. Triangular diagram showing three energy components, net radiation, sensible heat flux and latent heat flux, of the previous study in table 5.

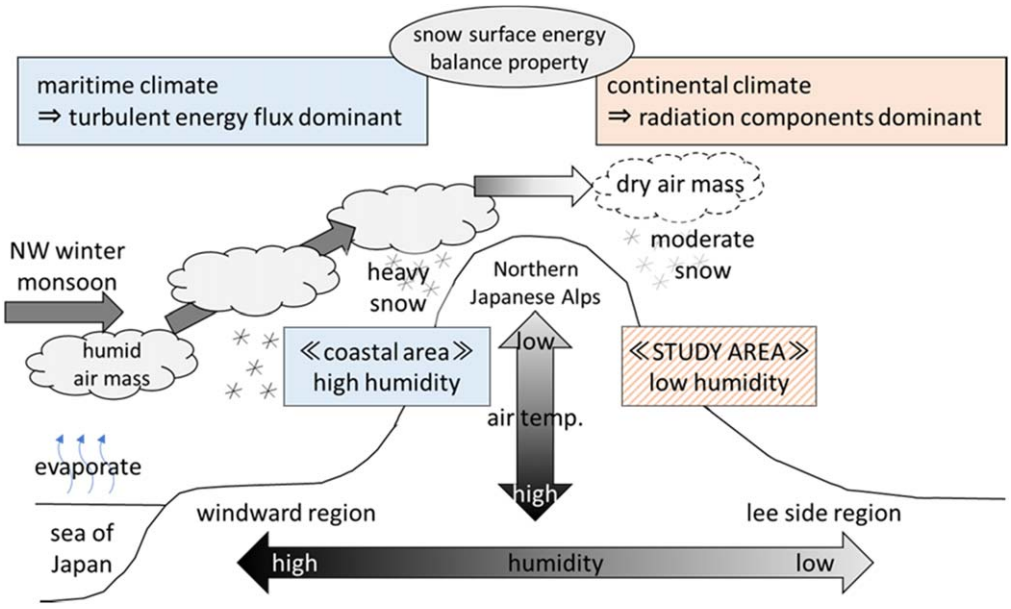

Figure 5. Mechanism that forms the specific atmospheric condition and the surface energy balance property in the Northern Japanese Alps.

(1) Siberian anticyclone formation on the East Eurasian continent in winter

(2) Cyclones in the Pacific Ocean

(3) Large amounts of heat and vapor from warm superficial Tsushima currents in the Sea of Japan (Kurooka 1957, Ninomiya 1968)

This mechanism is known as the representative Japanese winter monsoon. It yields heavy snowfall in the coastal areas because the humid air mass originating from the winter monsoon is forced to lift over the Northern Japanese Alps (Estoque and Ninomiya 1976). Precipitation rarely occurs in the island area due to typical meteorological conditions. There is an amount of precipitation gradient between the windward (north west) area and the lee side (south east) area of the Northern Japanese Alps. A precipitation gradient similar to that in the Northern Japanese Alps was reported by Viale *et al* (2019). It showed that an East-West precipitation gradient

in Patagonia, Chile made a distinction in climate between the windward area and the lee side area in the Andes Mountains. Moreover, Ikeda *et al* (2009) also showed that the climate condition in the lee side of the Northern Japanese Alps is dry, it is based on the snowpack observation of physical properties. The specificity of our surface energy balance analysis was established in addition to Ikeda *et al* (2009), the mechanism of snowfall in Japan, and the environment of seasonal snow cover.

4.2. Surface energy balance properties in Kamikochi, Norikura highland and Nishi-Hodaka

The topographic condition, surrounding vegetation, and elevation difference are specific surface energy balance properties in AWS-K, AWS-N, and AWS-H. AWS-K is located at the bottom of a valley terrain; a cold air pool is typically formed. When a cold air pool is formed, a stable stratification in the boundary layer and radiation cooling occurs, and sublimation of the snowpack further cooled the snow surface further. Snowpack cooling frequently occurs in the AWS-K. The surface energy balance property in AWS-N resembled that of in AWS-K. There is no distinct difference in air temperature and atmospheric specific humidity with AWS-K and AWS-N. However, the turbulent energy flux in AWS-N was smaller than that of in AWS-K. Surrounding vegetation allowed the wind speed to decrease, resulting in the increased formation of a stable boundary layer and restraining turbulence.

The differences in air temperature due to the atmospheric pressure and the amount of snowfall among in AWS-K, AWS-N, and AWS-H make the characteristic of surface energy balance in AWS-H. The major meteorological differences among AWS-K and AWS-N against AWS-H are as follows: in AWS-H, (1) a period in which the daily mean air temperature turns to be positive is later and (2) the snow-covered duration is longer than those in the AWS-K and AWS-N. Thus, significant snow ablation in AWS-H begins later and stronger snow melt occurred in the late ablation period than those in the other two sites. In addition, incoming shortwave radiation, air temperature, and atmospheric humidity increase with time. This consideration, therefore, reveals the characteristics of AWS-H, that is, net shortwave radiation and turbulent heat flux large in the late ablation period, and rapid snow ablation is occurred, as well as the difference in the surface energy balance properties among the three AWS sites located in the same climate region.

5. Conclusion

We discussed the surface energy properties of the Northern Japanese Alps, Kamikochi, Norikura highland, and Nishi-Hodaka. The surface energy balance property in this region was similar to that in the continental climate region because of the Japanese specific climate (winter monsoon) and topographic (steep elevation gradient) conditions of the Japanese Alps. The representative Japanese winter monsoon supplies warm and humid air masses to the Japanese Alps, resulting in heavy snowfall in the coastal areas. This forms a climate contrast between the windward and leeward areas of the Northern Japanese Alps. Therefore, we conclude that the seasonal snow cover on the lee side of the Northern Japanese Alps was formed under relatively dry atmospheric conditions. This is a new finding, considered with a surface energy balance analysis. Some areas in the Japanese Alps are dry, while the Japanese climate is usually regarded as a maritime climate.

There were some area-specific surface energy balance properties in Kamikochi, Norikura highland and Nishi-Hodaka. These properties were affected by the topographic conditions in Kamikochi, surrounding vegetation in the Norikura highland, and low air temperature conditions in Nishi-Hodaka due to the high elevation. The AWS sites are only approximately 10 km apart; however, a unique surface energy balance property was found for each site.

Acknowledgments

The outcomes of this study were obtained when the first author was attending a graduate program at Shinshu University, and all data used in this study are attributed to Shinshu University. We are grateful to everyone who supported this study. In addition, a part of this work (primarity data analysis) was conducted using resources from the Arctic Challenge for Sustainability II (ArCS II), Program Grant Number JPMXD1420318865. The Nishiho Mountain Lodge is thanked for their generous cooperation with our field survey. Meteorological data obtained by Shinshu University are publicly available in http://ims.shinshu-u.ac.jp/ (Japanese only). Some precipitation data observed by the Japan Meteorological Agency used in this research are from https://www.jma.go.jp/jma/indexe.html.

Data availability statement

The data generated and/or analysed during the current study are not publicly available for legal/ethical reasons but are available from the corresponding author on reasonable request.

ORCID iDs

Motoshi Nishimura https://orcid.org/0000-0003-3613-7546

References

Abermann J, As D V A N, Wacker S, Langley K, Machguth H and Fausto R S 2019 Strong contrast in mass and energy balance between a coastal mountain glacier and the Greenland ice sheet *J. Glaciol.* **65** 263–9
Andreas E L 1987 A theory for the scalar roughness and the scalar transfer coefficients over snow and sea ice *Bound.-Lay. Meteorol.* **38** 159–84
Andreassen L M, van Den Broeke M R, Giesen R H and Oerlemans J 2008 A 5 year record of surface energy and mass balance from the ablation zone of Storbreen Norway *J. Glaciol.* **54** 245–58
Arie K, Narama C, Fukui K, Iida H and Takahashi K 2019 Ice thickness and flow of the Karamatsuzawa perennial snow patch in the northern Japanese Alps *J. Jpn. Soc. Snow and Ice (Seppyo)* **81** 283–95 (in Japanese with English abstract)
Bintanja R 1995 The local surface energy balance of the ecology glacier King George Island Antarctica: measurements and modelling *Antarct. Sci.* **7** 315–25
Braithwaite R J and Olesen O B 1990 A simple energy-balance model to calculate ice ablation at the margin of the Greenland ice sheet *J. Glaciol.* **36** 222–8
Brazel A J, Tempe F B, Chambers D and Kalkstein L S 1992 Summer energy balance on West Gulkana Glacier Alaska and linkages to a temporal synoptic index *Z. Geomorph. Suppl. Bd.* **86** 15–34
van den Broeke M, van As D, Reijmer M and van de Wal R 2005 Sensible heat exchange at the Antarctic snow surface: a study with automatic weather stations *Int. J. Climatol.* **25** 1081–101
De La Casiniere A 1974 Heat exchange over a melting snow surface *J. Glaciol.* **13** 55–72
La Chapelle E R 1959 Annual mass and energy exchange on the Blue Glacier *J. Geophys. Res.* **64** 443–9
Cline D W 1997 Snow surface energy exchanges and snowmelt at a continental, midlatitude Alpine site *Water Resour. Res.* **33** 689–701
Cohen J and Rind A 1991 The effect of snow cover on the climate *J. Climate* **4** 689–706
Conway J P and Cullen N J 2016 Cloud effects on surface energy and mass balance in the ablation area of Brewster Glacier New Zealand *Cryosphere* **10** 313–28
Cullen N J and Conway J P 2015 A 22 month record of surface meteorology and energy balance from the ablation zone of Brewster Glacier New Zealand *J. Glaciol.* **61** 931–46
Datt P, Srivastava P K, Negi P S and Satyawali P K 2008 Surface energy balance of seasonal snow cover for snow-melt estimation in N-W Himalaya *J. Earth Syst. Sci.* **117** 567–73
Dyer A J 1974 A review of flux-profile relationships *Bound.-Lay. Meteorol.* **7** 363–72
Estoque M A and Ninomiya K 1976 Numerical simulation of Japan Sea effect snowfall *Tellus* **28** 243–53
Fukami H and Naruse R 1987 Ablation of ice and heat balance on Soler glacier *Patagonia Bull. Glacier Res.* **4** 37–42
Fukui K, Iida H and Kosaka T 2018 Newly identifying active glaciers in the Northern Japanese alps and their characteristics *Geogr. Rev. of Jpn. Ser.* A **91** 43–61
Föhn P M B 1973 Short-term snow melt and ablation derived from heat- and mass-balance measurements *J. Glaciol.* **12** 275–89
Giesen R H, Andreassen L M, Van Den Broeke M R and Oerlemans J 2009 Comparison of the meteorology and surface energy balance at Storbreen and Midtdalsbreen, two glaciers in southern Norway *Cryosphere* **3** 57–74
Giesen R H, van den Broeke M R, Oerlemans J and Andreassen L M 2008 Surface energy balance in the ablation zone of Midtdalsbreen, a glacier in southern Norway: interannual variability and the effect of clouds *J. Geophys. Res. Atmos.* **113** D21111
Gillett S and Cullen N J 2011 Atmospheric controls on summer ablation over Brewster Glacier, New Zealand *Int. J. Climatol.* **31** 2033–48
Giorgi F, Hurrell J W, Marinucci M R and Beniston M 1997 Elevation dependency of the surface climate change signal: a model study *J. Climate* **10** 288–96
Greuell W and Smeets P 2001 Variations with elevation in the surface energy balance on the Pasterze (Austria) *J. Geophys. Res. Atmos.* **106** 31717–27
Gądek B and Leszkiewicz J 2010 Influence of snow cover on ground surface temperature in the zone of sporadic permafrost Tatra Mountains, Poland and Slovakia *Cold Reg. Sci. Technol.* **60** 205–11
Hock R and Holmgren B 1996 Some aspects of energy balance and ablation of Storglaciären, northern Sweden *Geogr. Ann.* **78** 121–31
Hogg I G G, Paren J G and Timmis R J 1982 Summer heat and ice balances on Hodges glacier, South Georgia, Falklands Dependencies *J. Glaciol.* **28** 221–38
Ikeda S, Wakabayashi R, Izumi K and Kawashima K 2009 Study of snow climate in the Japanese Alps: comparison to snow climate in North America *Cold Reg. Sci. Technol.* **59** 119–25
Ishikawa N, Owens I F and Sturman A P 1992 Heat balance characteristics during fine periods on the lower parts of the Franz Josef Glacier, South Westland, New Zealand *Int. J. Climatol.* **12** 397–410
Kawase H, Suzuki C, Ishizaki N N, Uno F, Iida H and Aoki K 2015 Simulations of monthly variation in snowfall over complicated mountainous areas around Japan's Northern Alps *SOLA* **11** 138–43
Klok E J, Nolan M and Broeke M R V D 2005 Analysis of meteorological data and the surface energy balance of McCall Glacier, Alaska, USA *J. Glaciol.* **51** 451–61
Kondo J and Yamazawa H 1986 Bulk transfer coefficient over a snow surface *Bound.-Lay. Meteorol.* **34** 123–35
Konya K, Matsumoto T and Naruse R 2004 Surface heat balance and spatially distributed ablation modelling at Koryto Glacier, Kamchatka Peninsula, Russia *Geogr. Ann.* **86** 337–48
Kurooka H 1957 Modification of siberian the open air mass caused by flowing Japan out over sea surface of Northern Japan *J. Meteorol. Soc. Jpn. Ser. II* **35** 52–9
Liestøl O 1967 Storbreen Glacier in Jotunheimen, Norway *Norsk Polarinstitutt* **141** 1–63

Magono C, Kikuchi K, Kimura T, Tazawa S and Kasai T 1966 A study on the snowfall in the winter monsoon season in hokkaido with special reference to low land snowfall *J. Fac. Sci. Hokkaido Univ. Ser.* **2** 287–308
Marks D, Kimball J, Tingey D and Link T 1998 The sensitivity of snowmelt processes to climate condition and forest cover during rain-on-snow: a case study of the 1996 Pacific Northwest flood *Hydrol. Proc.* **12** 1569–87
Martin S 1975 Wind regimes and heat exchange on Glacier de Saint-Sorlin *J. Glaciol.* **14** 91–105
Matsumoto T, Kawashima K, Togari-Ohta A and Shimamura M 2010 Estimation of outflow from the bottom of a snowpack using a combination of a temperature-radiation index model and a percolation model *J. Jpn. Soc. Snow and Ice (Seppyo)* **72** 255–70 (in Japanese with English abstract)
Matthews T, Hodgkins R, Gudmundsson S, Pálsson F and Björnsson H 2015 Inter-decadal variability in potential glacier surface melt energy at Vestari Hagafellsjökull (Langjökull, Iceland) and the role of synoptic circulation *Int. J. Climatol.* **35** 3041–57
Messel S 1971 Mass and heat balance of Omnsbreen - a climatically dead glacier in southern Norway *Nor. Polarinst. Skr.* **156** p 43
Moore R D and Owens I F 1984 Controls on advective snowmelt in a maritime alpine basin *J. Clim. Appl. Meteorol.* **23** 135–42
Mott R, Daniels M and Lehning M 2015 Atmospheric flow development and associated changes in turbulent sensible heat flux over a patchy mountain snow cover *J. Hydrometeorol.* **16** 1315–40
Munro D S 1990 Comparison of melt energy computations and ablatometer measurements on melting ice and snow *Arct. Alp. Res.* **22** 153–62
Neale S M and Fitzharris B B 1997 Energy balance and synoptic climatology of a melting snowpack in the Southern Alps, New Zealand *Int. J. Climatol.* **17** 1595–609
Ninomiya K 1968 Heat and water budget over the Japan Sea and the Japan islands in winter season *J. Meteorol. Soc. Jpn.* **46** 343–72
Nishimura M, Sasaki A and Suzuki K 2018 Energy balance variation on the snow surface during the snow covered season in the norikura highland, Japanese Alpine Area *Bull. Glaciol. Res.* **36** 23–35
Nishimura M, Sasaki A and Suzuki K 2019 Long-term fluctuations, modelling and predictions of the snow accumulation and ablation process in norikura highland: study using an energy balance analysis and ablation models *J. Geogr. (Chigaku zasshi)* **128** 61–75 (in Japanese with English abstract)
Ogawa M and Nogami M 1994 Precipitation amount separated by precipitation type using discriminating temperature during winter season *J. Jpn. Soc. Hydrol. Water Res.* **7** 421–7 (in Japanese with English abstract)
Oguma H, Ide R, Amagai Y and Hamada T 2019 Using a time-lapse camera network to monitor alpine vegetation phenology and snowmelt times *J. Geogr. (Chigaku zasshi)* **128** 93–104 (in Japanese with English abstract)
Poggi A 1977 Heat balance in the ablation area of the ampere glacier (Kerguelen Islands) *J. Appl. Meteorol.* **16** 48–55
Reijmer C, Greuell W and Oerlemans J 1999 The annual cycle of meteorological variables and the surface energy balance on Berkner Island Antarctica *Ann. Glaciol.* **29** 49–54
Schneider C, Kilian R and Glaser M 2007 Energy balance in the ablation zone during the summer season at the Gran Campo Nevado Ice Cap in the Southern Andes *Global Planet. Change* **59** 175–88
Sicart J E, Hock R and Six D 2008 Glacier melt, air temperature, and energy balance in different climates: the Bolivian Tropics, the French Alps, and northern Sweden *J. Geophys. Res. Atmos.* **113** D24113
Sicart J E, Wagnon P and Ribstein P 2005 Atmospheric controls of the heat balance of Zongo Glacier (16° S, Bolivia) *J. Geophys. Res. Atmos.* **110** 1–17
Streten N A and Wendler G 1968 The Midsummer Heat Balance of an Alaskan Maritime Glacier *J. Glaciol.* **7** 431–40
Suzuki K 2017 Variation trend of stream runoff in the Japanese Alps catchment *J. Japanese Assoc. Hydrol. Sci.* **47** 87–96
Suzuki K 2018 Variations in climatic and hydrologic trends in the Kamikochi region of the Japanese Alps *J. Jpn. Soc. Snow and Ice (Seppyo)* **80** 103–13
Suzuki K and Sasaki A 2019 Meteorological observations in the Japanese Alps region *J. Geogr. (Chigaku Zassi)* **128** 9–19 (in Japanese with English abstract)
Takeuchi Y, Satow K, Naruse R, Ibarzabal T, Nishida K and Kenichi M 1995a Meteorological feature at Moreno and Tyndall glaciers, Patagonia, in the summer 1993/94 *Bull. Glaciol. Res.* **13** 35–44
Takeuchi Y, Naruse R and Satow K 1995b Characteristics of heat balance and ablation on Moreno and Tyndall glaciers, Patagonia, in the summer 1993/94 *Bull. Glacier Res.* **13** 45–56
Viale M, Bianchi E, Cara L, Ruiz L E, Villalba R, Pitte P and Zalazar L 2019 Contrasting climates at both sides of the Andes in Argentina and Chile *Front. Environ. Sci.* **7** 1–15
van de Wal R S W, Oerlemans J and van der Hage J C 1992 A study of ablation variations on the tongue of Hintereisferner, Austrian Alps *J. Glaciol.* **38** 319–24
Wendler G and Streten N A 1969 A short term heat balance study on a coast range glacier *Pure Appl. Geophys.* **77** 68–77
Willis I C, Arnold N S and Brock B W 2002 Effect of snowpack removal on energy balance, melt and runoff in a small supraglacial catchment *Hydrol. Proc.* **16** 2721–49